







Learning Multiparametric Biomarkers for Assessing MR-Guided Focused Ultrasound Treatment of Malignant Tumors

Blake E. Zimmerman , Sara Johnson , Henrik Odéen , Jill Shea , Markus D. Foote , Nicole Winkler, Sarang C. Joshi, Allison Payne 

Abstract—Noninvasive MR-guided focused ultrasound (MRgFUS) treatments are promising alternatives to the surgical removal of malignant tumors. A significant challenge is assessing the viability of treated tissue during and immediately after MRgFUS procedures. Current clinical assessment uses the nonperfused volume (NPV) biomarker immediately after treatment from contrast-enhanced MRI. The NPV has variable accuracy, and the use of contrast agent prevents continuing MRgFUS treatment if tumor coverage is inadequate. This work presents a novel, noncontrast, learned multiparametric MR biomarker that can be used during treatment for intratreatment assessment, validated in a VX2 rabbit tumor model. A deep convolutional neural network was trained on noncontrast multiparametric MR images using the NPV biomarker from follow-up MR imaging (3-5 days after MRgFUS treatment) as the accurate label of nonviable tissue. A novel volume-conserving registration algorithm yielded a voxel-wise correlation between treatment and follow-up NPV, providing a rigorous validation of the biomarker. The learned noncontrast multiparametric MR biomarker predicted the follow-up NPV with an average DICE coefficient of 0.71, substantially outperforming the current clinical standard (DICE coefficient = 0.53). Noncontrast multiparametric MR imaging integrated with a deep convolutional neural network provides a more accurate prediction of MRgFUS treatment outcome than current contrast-based techniques.

Index Terms—machine learning, ablation therapy, deformable image registration, convolutional neural network

I. INTRODUCTION

Minimally and noninvasive ablation therapies for treatment of different pathologies have become promising alternatives to surgical resection. Ablation treatments are currently applied to several indications, including prostate disease [1]–[3], uterine fibroids [4]–[6], bone metastases [7], [8], liver

[9], [10], and breast [11], [12]. Magnetic-resonance-guided focused ultrasound (MRgFUS) is a noninvasive ablation treatment. An essential component of MRgFUS procedures is accurately monitoring the treatment in real time and assessing the viability of ablated tissue immediately after the procedure [12]. MR provides excellent soft tissue contrast for all phases of MRgFUS procedures, including treatment planning, real-time temperature monitoring, and treatment assessment. MR biomarkers derived from MR imaging are used to assess the extent of treated tissue. If untreated tissue is detected, then additional ablation needs to be performed [12].

The most common MR biomarker for assessing treated tissue is the nonperfused volume (NPV) [12], [13] that is derived from contrast-enhanced (CE) T1-weighted (T1w) MR imaging. The NPV is characterized by a lack of signal enhancement from impaired blood flow due to vascular damage and coagulation from MRgFUS ablation [12], [14]–[16]. However, the NPV biomarker obtained immediately after MRgFUS ablation treatment is not reliable for assessing the extent of the treated region due to confounding treatment effects that directly affect tissue perfusion such as edema, hyperemia, and increased vascular permeability [12]. Additionally, continuing treatment after CE imaging inhibits further treatment monitoring and can trap toxic contrast agent in the tissue, prohibiting further MRgFUS treatment if viable tumor tissue is detected [12], [17], [18]. The need is critical for noncontrast MR biomarkers that can accurately assess tissue viability during and immediately after treatment without inhibiting further MRgFUS ablation.

Several noncontrast, immediate MR biomarkers from multiparametric MR (MPMR) imaging have been investigated to assess MRgFUS immediately after treatment, including T2w images, MR temperature imaging (MRTI), and apparent diffusion coefficient (ADC) maps [1], [13], [19]–[21]. These acute MR biomarkers are based on intrinsic tissue properties that are sensitive to MRgFUS-induced changes [12]. However, the nonlinear relationship between MRgFUS-induced tissue property changes and tissue viability is unknown. Supervised machine learning provides a flexible platform to learn a nonlinear mapping between immediate MR biomarkers and tissue viability. Using the learned non-linear relationship would provide accurate treatment assessment during and immediately after MRgFUS treatments using noncontrast MR biomarkers.

Supervised machine learning requires an accurate label of tissue viability. The NPV acquired immediately after MRg-

Manuscript compiled October 1, 2020. This work was supported by the National Institutes of Health [5R37CA224141, S10OD018482, 1R03EB026132]

B. E. Zimmerman, M. D. Foote, and S. C. Joshi are with the Scientific Computing and Imaging Institute, and also with the Department of Biomedical Engineering, University of Utah, Salt Lake City, UT 84112 USA.

S. Johnson is with the Department of Biomedical Engineering, University of Utah, Salt Lake City, UT 84112 USA.

B. E. Zimmerman, S. Johnson, H. Odéen, and A. Payne are with the Utah Center for Advanced Imaging Research, University of Utah, Salt Lake City, UT, USA.

S. Johnson, H. Odéen, and A. Payne and N. Winkler are with the Department of Radiology and Imaging Sciences, University of Utah, Salt Lake City, UT, USA

J. Shea is with the Department of Surgery, University of Utah, Salt Lake City, UT 84112 USA.

This is the author's version of the accepted paper. The publisher's copy may be accessed from IEEE by the DOI 10.1109/TBME.2020.3024826

arXiv:1910.10769v2 [eess.IV] 29 Sep 2020

FUS ablation does not accurately identify tissue viability due to transient physiological changes. Alternatively, the NPV biomarker 3-5 days after MRgFUS treatment (follow-up NPV) is a more accurate label of tissue viability [9], [14], [15]. This follow-up NPV could be used as a label for nonviable tissue to facilitate learning MPMR biomarkers for immediate MRgFUS treatment assessment. However, this follow-up NPV is not aligned with the immediate MPMR biomarkers due to changes in patient pose, positioning, and tissue deformation. Image registration is necessary to account for changes in subject pose and positioning to provide a spatially accurate label of nonviable tissue for supervised machine learning.

Image registration has been an active research area for the analysis of longitudinal imaging, and numerous image registration algorithms have been proposed in the literature [21]–[26]. The objective of longitudinal registration is to correct for changes in patient position and pose between imaging sessions. The volume of tissues such as muscle, fat, and bone is preserved under normal physiological loading, such as the changes in patient position and pose [27]. Additionally, over the first 3-5 days, minimal tissue reabsorption and healing processes after MRgFUS ablation do not result in a measurable change in tissue volume [28]. A volume-conserving registration must be implemented to ensure registration does not introduce artificial changes in the ablation volume in 3-5 day MR images. Algorithms presented in the literature regularize volume change during registration, but they do not strictly enforce volume conservation [25], [26], [29]. To our knowledge, no publicly available volume conserving image registration pipeline exists.

A longitudinal registration method that strictly enforces volume preservation is needed to allow for accurate correction of pose and positioning deformations that occur between follow-up NPV and immediate MPMR images. To address the specialized registration need, we developed **AVOCADO: A VOLUME CONSERVING ALGORITHM FOR DIFFEOMORPHISMS**, a longitudinal registration pipeline that computes a volume-preserving deformation. AVOCADO aligns the follow-up NPV with the immediate MPMR images to yield a spatially accurate label of nonviable tissue.

This work utilizes this novel registration pipeline to evaluate a **MULTIPARAMETRIC BIOMARKER CONVOLUTIONAL NEURAL NETWORK (MPB-CNN)**, a deep learning model for predicting nonviable versus viable tissue from immediate MPMR imaging. The resulting label of nonviable tissue from AVOCADO is used to train MPB-CNN to predict the nonviable tissue from immediate MPMR images without a contrast agent. These new techniques are demonstrated using *in vivo* data of a preclinical rabbit VX2 rabbit tumor model.

II. STUDY DESIGN

A rabbit tumor model [30] was used to generate a data set with and without contrast biomarkers to compare MPB-CNN against the clinical biomarker (NPV obtained immediately after treatment). The ablation procedure and associated imaging protocol were designed to capture MPMR and structural anatomical images (noncontrast T1w) at distinct

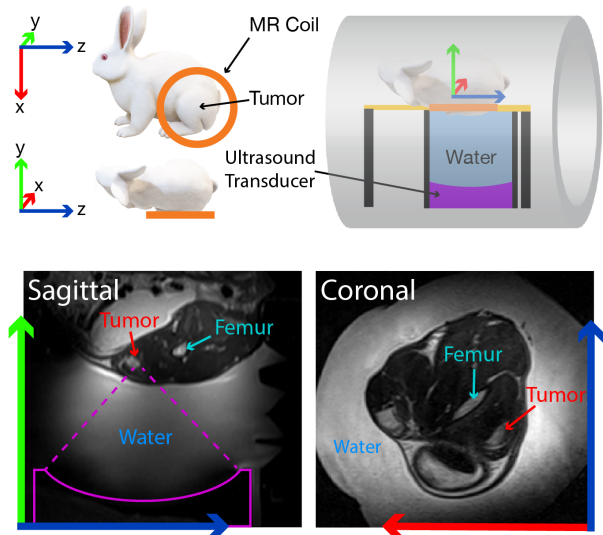


Fig. 1: The top row shows the positioning of the rabbit in the MR bore and relative to the ultrasound transducer. The radiofrequency receiver MRI coil incorporated in the MR table is shown in orange relative to the animal quadriceps. The bottom row shows examples of the acquired T2-weighted images in relation to the overall setup. The colored arrows along each image indicate the MR direction.

time points throughout the procedure. MPMR images were acquired before, during, and after MRgFUS ablation treatment to generate the immediate MPMR biomarker images. CE T1w MR images were collected following the MPMR imaging protocol at the end of the MRgFUS ablation procedure and used to generate the clinical biomarkers. Following MRgFUS ablation, the animal recovered for 3-5 days post-treatment, and follow-up imaging, including the MPMR protocol and CE-T1w MR imaging, was performed to generate the follow-up NPV label of nonviable tissue. The specifics of the animal tumor model, ablation parameters, and image acquisitions are described below. The University of Utah Institutional Animal Care and Use Committee approved all procedures (#17-08012, September 7, 2017).

A. Animal Model and Hardware

A VX2 (5×10^6 cells in 50% media/Matrigel) cell suspension was injected intramuscularly into both quadriceps of New Zealand white rabbits (N=8). On MRgFUS treatment day, the animal was anesthetized with a ketamine/xylazine injection (IM, 25/5 mg/kg) and intubated. Anesthesia was maintained with inhaled isoflurane (0.5-4.0%). Under anesthesia, hair was removed via clippers and a depilatory cream (Nair™) was applied to obtain an appropriate acoustic window for treatment. Using a preclinical MRgFUS system (Image Guided Therapy, Inc., Pessac, France), ablation was performed on one tumor and surrounding muscle tissue with a 256-element phased-array transducer (Imasonic, Voray-sur-l’Ognon, France; 10-cm focal length, 14.4 x 9.8 cm aperture, $f = 940$ kHz, $1.8 \times 2.5 \times 10.2$ mm full width half maximum size of the intensity profile as measured in water via hydrophone (HNR-1000, Onda, Sunnyvale, CA)) inside a 3T MRI scanner (PrismaFIT Siemens, Erlangen, Germany). At 3-5 days post-treatment, the animal

TABLE I: Parameters for the multiparametric scanning sequence used for ablation day and follow-up imaging. Coronal orientation was used for all MR acquisitions. TR: Repetition Time, TE: Echo Time, EPI: Echo Planar Imaging, SPACE: Sampling Perfection with Application Optimized Contrasts Using Different Flip Angle Evolution, VIBE: Volumetric Interpolated Breath-Hold, GRE: Gradient Recalled Echo, MRTI: Magnetic Resonance Temperature Imaging, SS: Single Shot, SE: Spin Echo, and ETL: Echo Train Length. * T1w sequence with contrast for NPV segmentation. ** T1w sequence without contrast for image registration.

Scan Type	Sequence	TR (ms)	TE (ms)	Flip Angle	Field of View (mm)	Pixel Bandwidth (Hz/Pixel)	Acquisition Resolution (mm)	Number Averages	Acquisition Time (mm:ss.ms)
MRTI	GRE-EPI (ETL=7)	25	11	14°	192×150×20	750	1.5×1.5×2.0	1	0:04.50
T1w*	VIBE	7.19	2.05	15°	256×192×52	250	1.0×1.0×1.0	1	1:03.00
T2w	SPACE	2000	300	120°	256×192×52	700	1.0×1.0×1.0	2	5:12.00
T1w**	VIBE	7.19	2.52	15°	256×192×56	250	0.5×0.5×1.0	3	6:19.00
Diffusion	SS-SE-EPI (ETL=92) (b=20,500)	7500	117	90°	160×116×20	1260	1.25×1.25×2.0	1	1:38.00

was anesthetized and follow-up MR imaging was obtained (Table I). A depiction of the setup can be seen in Figure 1.

B. Ablation Parameters

Each animal received a mean of 11 sonications (range: 8-14) during the MRgFUS ablation procedure, with a mean acoustic power of 47 W (range: 30-69 W) and an average sonication duration of 31 seconds (range: 15-40 seconds), for an average total output energy of 17,665 J (range: 11,563-26,004 J). The number of sonications, power output, tumor volume, and total output energy are shown in Table II for each subject. The resulting lesion sizes have large variations due to subject-specific factors including inadequate acoustic coupling with residual hair in the ultrasound path, reflection and refraction issues due to the location of the tumor with respect to bone, beam reflection due to the incidence angle of ultrasound with the skin, heterogeneous acoustic tissue properties including assumed low tumor attenuation, and animal motion. All FUS sonications were monitored in real time with a 3D MRTI gradient echo sequence with a segmented echo planar imaging readout (Table I).

C. Image Acquisition

A custom, single-loop radiofrequency MR receiver coil was incorporated into the MRgFUS treatment table to improve the signal to noise ratio (SNR) of the MR imaging (Figure 1).

TABLE II: Ablation details for each subject including number of ablation points, acoustic power output and total energy used for each subject.

Subj.	Tumor Vol.(mm^3)	Number of Sonications	Acoustic Power Mean \pm 1 Std. (W)	Total Energy (kJ)
1	1477.5	11	36 \pm 18	16.50
2	757.0	13	30 \pm 8	11.23
3	785.5	11	57 \pm 17	23.14
4	594.5	10	38 \pm 5	12.74
5	858.5	8	44 \pm 7	11.56
6	248.1	12	69 \pm 18	26.00
7	1929.5	14	44 \pm 9	18.59
8	806.4	10	56 \pm 9	18.55

MPMR images were acquired at three distinct time points: pre-ablation, immediately post-treatment, and 3-5 days post-treatment (follow-up). The details of each scan collected at each time point are outlined in Table I. In addition to collecting a T1w image at each time point without contrast, the same sequence was acquired immediately (\sim 30 seconds) after administering gadolinium contrast after ablation on treatment day and at the end of follow-up imaging 3-5 days post-treatment. The CE T1w images were collected to generate the NPV biomarker both immediately after and 3-5 days post-treatment. The NPVs were generated by semiautomatic segmentation of the CE images and were validated by an expert radiologist (NW). The high-resolution T1w image without contrast acquired at all time points depicts the quadriceps anatomy without showing the tumor or ablated regions and can therefore be used for registration without biasing the registration with the tumor or ablated regions.

III. REGISTRATION METHODS

For completeness, we describe the specialized registration that was developed to facilitate the MPB-CNN prediction of tissue viability. For the described data set in section II, the source image is the noncontrast T1w MR image acquired during follow-up imaging, and the target image is the noncontrast T1w MR image acquired immediately after the MRgFUS ablation procedure. The noncontrast images do not include intensity features of the tumor or ablation sites, making the intensity-based registration unbiased to these features. Registration estimates a high-dimensional spatially smooth one-to-one and onto transformation, or a diffeomorphism, that maps the locations from a source image to a target image, specifically: $\phi: \Omega \subset \mathbb{R}^3 \rightarrow \Omega$. AVOCADO utilizes a multiscale gradient flow that is driven first by discrete landmarks and then by image intensity. Helmholtz-Hodge decomposition is used to guarantee volume conservation. These sequential steps result in a volume-preserving diffeomorphism that accurately maps the follow-up NPV biomarker to the immediate MPMR images. This accurate voxel-wise registration enables training MPB-CNN to generate an immediate MPMR biomarker to

assess the extent of MRgFUS ablation treatments without contrast imaging.

A. Gradient Flow

A multiscale algorithm was developed for generating a diffeomorphism that maps two anatomies based on the gradient flow methodology previously used for general image registration problems [31]–[35]. A diffeomorphism is constructed in terms of solutions to the Lagrangian transport equation, defined via the ordinary differential equation (ODE)

$$\frac{d\phi(\vec{x}, t)}{dt} = v(\phi(\vec{x}, t), t), \quad \phi(\vec{x}, 0) = \vec{x}, \quad t \in [0, 1] \quad (1)$$

where \vec{x} is position, t is time, and $v(x, t)$ is a time-varying velocity vector field. The diffeomorphism $\phi(\cdot, \cdot)$ at time point t is controlled by the velocity field $v(x, t)$ via the associated integral equation

$$\phi(\vec{x}, t) = \vec{x} + \int_0^t v(\phi(\vec{x}, \tau), \tau) d\tau, \quad x \in \Omega. \quad (2)$$

If the velocity field is sufficiently well behaved [36], [37], $\phi(\vec{x}, t)$ is guaranteed to be a diffeomorphism. The inverse diffeomorphism $\phi^{-1}(\vec{x}, t)$ satisfies the Eulerian ODE given by

$$\frac{d\phi^{-1}(\vec{x}, t)}{dt} = -D[\phi^{-1}(\vec{x}, t)] v(\phi^{-1}(\vec{x}, t), t) \quad (3)$$

where $D[\cdot]$ is the Jacobian. The above ODE can be approximately integrated via an implicit Euler method:

$$\phi^{-1}(\vec{x}, t + \delta_t) = \phi^{-1}(x - \delta_t v(\vec{x}, t), t) \quad (4)$$

where δ_t is a scalar time step.

Using the transport equation above, a gradient flow is developed, governed by forcing functions $g(x, t)$. The forcing functions are the gradient of an energy potential that defines the registration problem. A forcing function $g(x, t)$ is related to the velocity field via

$$Lv(\phi(\vec{x}, t)) = g(\phi(\vec{x}, t)) \quad (5)$$

where L is a partial differential operator that has an associated smoothing kernel K such that

$$v(\phi(\vec{x}, t)) = Kg(\phi(\vec{x}, t)). \quad (6)$$

The operator K ensures the fields $v(x, t)$ are smooth and gives sufficient differentiability for the existence and uniqueness of the solution to the ODE, which guarantees that $\phi(\vec{x}, t)$ is a diffeomorphism [32]. Properties of the final diffeomorphism can be controlled via the properties of v at every time step.

B. Helmholtz-Hodge Decomposition

Under normal physiological tissue loading, soft tissues exhibit incompressible behavior due to high water volume fractions [27]. Enforcing that the velocity fields $v(x, t)$ in Equation (2) describe incompressible fluid flow ensures that the diffeomorphism is volume preserving. Mathematically, incompressibility is equivalent to ensuring the divergence of $v(x, t)$ is zero: $\nabla \cdot v(x, t) = 0$ [38]. According to the Helmholtz-Hodge decomposition, a smooth and rapidly decaying vector field can be uniquely decomposed into an orthogonal sum of an irrotational, or curl-free, vector field and a solenoidal, or divergence-free, vector field [39]. Uniquely decomposing the

velocity field $v(x, t)$ allows the calculation of the solenoidal component by removing the irrotational component, which projects $v(x, t)$ into the space of divergent-free vector fields [40]. By enforcing that each velocity field governing the ODE in Equation (1) is divergent free with the Helmholtz-Hodge decomposition, the deformation is constrained to be volume preserving and models realistic soft tissue deformation.

The Helmholtz-Hodge decomposition and vector field projection of a discretized velocity field is implemented in the Fourier domain. A vector field is projected to the space of solenoidal vector fields by removing the curl-free component:

$$\vec{F}_{curl} v(\vec{\omega}) = \vec{F}_v(\vec{\omega}) - \left(\frac{\vec{W}(\vec{\omega}) \cdot \vec{F}_v(\vec{\omega})}{\|\vec{W}(\vec{\omega})\|} \right) \frac{\vec{W}(\vec{\omega})}{\|\vec{W}(\vec{\omega})\|}. \quad (7)$$

where $\vec{W}(\cdot)$ is the Discrete Fourier Transform (DFT) of the discrete gradient operator and $\vec{\omega}$ is the angular frequency. The inverse DFT of $F_{curl} v(\vec{\omega})$ gives a divergent-free velocity field $v(x, t)$ for solving Equation (1). Controlling the divergence of the velocity field at every iteration generates a final diffeomorphism with physiologically expected incompressibility. Additionally, the incompressibility can be spatially modulated using a spatially varying convex combination of the original velocity field and the projected velocity field as follows:

$$v(x, t) = (1 - \alpha(x)) v_{orig}(x, t) + \alpha(x) v_{divfree}(x, t) \quad (8)$$

where $v(x, t)$ is the final velocity field, $v_{orig}(x, t)$ is the original unconstrained velocity field and $v_{divfree}(x, t)$ is the projected divergence free velocity field. When $\alpha(x) = 1$, the original volume is conserved point wise over the entire image domain. This study utilized $\alpha(x) = 1$.

An example of registration both with and without incompressibility can be seen in Fig. 2. The top row shows the source and target images and their respective starting areas (A) in units of pixels (px). The middle row shows the result of registration *without* projecting the velocity field $v(x, t)$ to the space of divergent-free velocity fields. The area of the source object is reduced by 32.87% to match the target area. However, if the ellipse is a biological tissue, then the area should remain constant through registration because tissues are incompressible. The bottom row shows the volume-preserving result of registration with projecting the velocity field $v(x, t)$ to the space of divergent-free velocity fields. The volume-preserving method generates deformations that reflect the incompressibility of biological tissues.

C. Rigid Registration

In the outlined study design, exactly replicating subject pose between treatment and follow-up imaging was impossible. For large changes in the subject pose, AVOCADO registration begins with a landmark registration problem based on user-defined source and target anatomical landmarks selected in follow-up and treatment-day coordinates, respectively. Anatomical landmarks are used to estimate a volume-preserving rigid transformation in two steps. First, an affine transformation A is estimated via a least squares minimization:

$$A = (\vec{c}_i \vec{p}_i^T) (\vec{p}_i \vec{p}_i^T)^{-1} \quad (9)$$

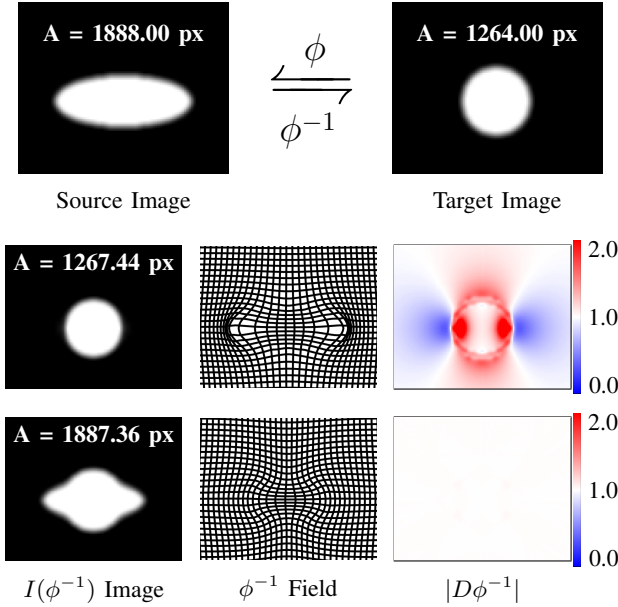


Fig. 2: Example of non-volume-preserving versus volume-preserving gradient flow registration. The top row shows the source and target image with their respective areas (A) in pixels. The middle and bottom rows from left to right show the deformed image, deformation field, and Jacobian determinant for non-volume-preserving (middle row) and volume-preserving registration (bottom row), respectively.

where \vec{p}_i are the source landmarks and \vec{c}_i are the target landmarks. Second, the affine transformation is projected to a rigid transformation R via the singular value decomposition of the matrix A [41].

D. Landmark-Driven Gradient Flow

Given the rigid transformation R , an anatomical landmark-driven higher dimensional transformation is estimated by using gradient flow on an energy potential $g(x) = E_{RBF}$, from Equation (5), which is a function only of the landmark points:

$$E_{RBF} = \sum_{i=1}^M \|R\vec{p}_i - \phi^{-1}(\vec{c}_i, t)\|^2 \quad (10)$$

where M is the number of landmark pairs and $\phi^{-1}(\cdot, t)$ is the inverse diffeomorphism at time t . A multiquadratic radial basis function (RBF) is used as the smoothing operator K :

$$K(\vec{r}) = \sqrt{1 + (\epsilon \vec{r})^2}, \quad \vec{r} = \vec{x} - \vec{c} \quad (11)$$

where ϵ is a shape-tuning parameter, set to $\epsilon = 1.0$ for all experiments in this work. Although thin plate splines are commonly used, they are ill-conditioned without an affine transformation. However, an affine transformation is not volume preserving. The velocity field $v(x, t)$ is expressed as a summation of weighted RBF fields. Given the distance d between points $\vec{d}_i = R\vec{p}_i - \phi^{-1}(\vec{c}_i, t)$, the weights b are solved via

$$\begin{bmatrix} b_1(t) \\ \vdots \\ b_i(t) \end{bmatrix} = \begin{bmatrix} K(\vec{r}_{11}) & \dots & K(\vec{r}_{1j}) \\ \vdots & \ddots & \vdots \\ K(\vec{r}_{i1}) & \dots & K(\vec{r}_{ij}) \end{bmatrix}^{-1} \begin{bmatrix} \vec{d}_1(t) \\ \vdots \\ \vec{d}_i(t) \end{bmatrix} \quad (12)$$

with $\vec{r}_{ij} = \phi^{-1}(\vec{c}_i, t) - \phi^{-1}(\vec{c}_j, t)$ [42]. The velocity field is given by

$$v(\vec{x}, t) = \sum_{i=1}^M b_i(t) K(\|\vec{R}\vec{x} - \vec{c}_i\|) \quad (13)$$

The vector field $v(\vec{x}, t)$ is subsequently projected into the space of divergent-free vectors fields via the Helmholtz-Hodge decomposition described in section III-B. For a given time step, the diffeomorphism ϕ^{-1} is updated via

$$\phi^{-1}(\vec{x}, t + \delta_t) = \phi^{-1}(\vec{x} - \delta_t v(\vec{x}, t), t) \quad (14)$$

where δ_t is a scalar step size. For a given time step, we update the diffeomorphism according to Equation (4) until a convergence criterion is met. For matching landmarks, the convergence point is when the E_{RBF} becomes less than the average interuser variability (ϵ_u) of selecting the landmarks, which is determined from the test-retest capability of users when selecting the source anatomical landmarks (section IV-A).

E. Image Intensity-Driven Gradient Flow

The final registration step is an image registration problem to match two anatomies based on image similarities of a source and target image. The image intensity-driven gradient flow is initialized with the diffeomorphism from landmark-driven gradient flow. The energy potential E_{Image} for the image registration problem is

$$E_{Image} = \int_{\Omega} \|I_1(\phi^{-1}(\vec{x}, t)) - I_0(\vec{x})\|^2 \quad (15)$$

where I_1 is the source image (follow-up, noncontrast T1w VIBE image) and I_0 is the target image (treatment-day, noncontrast T1w VIBE image). The associated forcing function from Equation (5) is given by

$$g(\vec{x}, t) = (I_1(\phi^{-1}(\vec{x}, t)) - I_0(\vec{x})) \nabla I_1(\phi^{-1}(\vec{x}, t)) \quad (16)$$

where ∇ is the gradient operator.

An operator of the Cauchy-Navier type is chosen for the L operator from Equation (5) with $L = -\alpha\Delta + \gamma I$, where Δ is the Laplace operator and I is the identity operator. The scalars α and γ control smoothness and ensure the operator is nonsingular, respectively. This operator has been used previously in image registration [43]. The smoothing kernel associated with L is applied in the Fourier domain with $\text{DFT}\{K\} = \text{DFT}\{L\}^{-1}$ to get $v(x, t)$. The smoothed vector field is projected into the space of divergent-free vector fields using the Helmholtz-Hodge decomposition described in section III-B. For a given time step, the diffeomorphism is updated according to Equation (4). The intensity-based registration continues until the change in energy E_{Image} in Equation (15) from the previous iteration is less than $\epsilon_I = 3 \times 10^{-4}$.

In total, the final diffeomorphism defined by AVOCADO is the composition of the rigid transformation, the gradient flow on anatomical landmarks, and the gradient flow on the image intensities. An outline of the final algorithm is shown in Figure 3. This volume-preserving method ensures that registration process does not bias the volume of the follow-up NPV biomarker.

```

1: procedure AVOCADO( $p_i, c_i, I_0, I_1, \delta_t$ )
2:   Solve affine  $A = (c_i p_i^T) (p_i p_i^T)^{-1}$ 
3:   Singular Value Decomposition  $A \mapsto R$ 
4:    $\phi_{RBF}^{-1}(\vec{x}, k=0) := \vec{x}$ 
5:   while  $E_{RBF} \geq \epsilon_u, k = k + 1$  do
6:     Solve spline weights  $b = K^{-1}d$ 
7:      $v(\vec{x}, k) = \sum_{i=1}^M b_i K(\|R\vec{x} - \phi^{-1}(\vec{c}_i, k)\|)$ 
8:     Project div-free  $\delta_t v(\vec{x}, k) \mapsto s(\vec{x}, k)$ 
9:      $\phi_{RBF}^{-1}(\vec{x}, k+1) = \phi_{RBF}^{-1}(\vec{x} - s(\vec{x}, k), k)$ 
10:  end while
11:   $\phi_I^{-1}(\vec{x}, k=0) = \phi_{RBF}^{-1}(\vec{x}, k)$ 
12:  while  $|E_{Image}(k-1) - E_{Image}(k)| \leq \epsilon_I$  do
13:     $g(\vec{x}, k) = (I_1(\phi_I^{-1}(\vec{x}, k)) - I_0) \nabla I_1(\phi_I^{-1}(\vec{x}, k))$ 
14:     $v(\vec{x}, k) = DFT^{-1}\{DFT\{L\}^{-1}DFT\{g(\vec{x}, k)\}\}$ 
15:    Project div-free  $\delta_t v(\vec{x}, k) \mapsto s(\vec{x}, k)$ 
16:     $\phi_I^{-1}(\vec{x}, k+1) = \phi_I^{-1}(\vec{x} - s(\vec{x}, k), k)$ 
17:  end while
18:  return  $\phi_I^{-1}(\vec{x}, k)$ 
19: end procedure

```

Fig. 3: AVOCADO algorithm to calculate the diffeomorphism $\phi^{-1}(\vec{x})$ mapping two anatomies I_1 and I_0 while preserving volume.

IV. REGISTRATION VALIDATION

To ensure the accuracy and volume preservation of our registration method, we describe the methods to assess different aspects of the AVOCADO algorithm. The accuracy and volume preservation of our method will be compared with a state-of-the-art registration method.

A. Landmark-Based Registration Accuracy

The overall accuracy of AVOCADO will be evaluated using manually selected anatomical landmarks. Multiple observers ($N=3$) were given anatomical landmarks in the target images and asked to find the corresponding landmarks in the source images using 3D Slicer software [44]. Ten source and target landmark pairs were chosen for each subject over the entire region of interest. Examples of the validation landmarks can be seen in Figure 4. The TRE was calculated by deforming anatomical landmarks with the estimated deformation and computing the Euclidean distance between the deformed point and its corresponding target landmark. The landmarks for validation were chosen independently from the RBF initialization landmarks.

The landmark-based accuracy of AVOCADO was compared with another leading, general purpose registration algorithm to demonstrate the overall accuracy of AVOCADO. Deformable Registration via Attribute Matching and Mutual-Saliency Weighting (DRAMMS) is the leading registration method for longitudinal registration. DRAMMS has been shown to consistently outperform other registration methods. In previous publications, DRAMMS has outperformed 12 competing registration methods, including ANTS and Demons, in overall target registration error and region similarity measures [22], [25], [45], [46]. To test the relative accuracy, DRAMMS was executed on the same noncontrast registration images used during the AVOCADO pipeline with default input parameters. The resulting volume change and the TRE were computed to

compare DRAMMS with AVOCADO. A two-sample-related t-test on the Euclidean error between deformed and target landmarks was used to test for a significant difference between DRAMMS and AVOCADO.

The error due to user variability when manually selecting anatomical landmarks was evaluated. Multiple observers selected validation landmarks, and each observer was asked to repeat their landmark selection. The inter- and intra-observer variations were calculated by comparing the Euclidean distance between selected landmarks both across observers and within a single observer, respectively. A two-sample-related t-test between inter- and intra-observer errors was used to test for significance difference between the same observer and across observers.

B. Changes in User-Dependent Inputs

AVOCADO is dependent on the input anatomical landmarks for rigid and RBF transformations. Due to manual user selection, variance is expected in the initialization landmarks introduced by the user's ability to select the anatomical landmarks. The robustness of AVOCADO to changes in the input landmarks was tested by applying a range of zero mean, normally distributed perturbations to each source landmark individually and executing the registration with the updated landmarks. Changes less than the re-test capability of the observers (intraobserver error) should not change the final registration accuracy.

C. Volume Preservation Capability

Transformations produced from AVOCADO should preserve volume when applied to follow-up MR imaging. The volume preservation capability of our model was validated using expert segmentations of the NPV biomarker on follow-up MR imaging [29]. The volume was calculated by integrating the binary segmentation and scaling by the product of the voxel spacing. The estimated deformation was then applied to the follow-up NPV segmented images to register them with the MR images obtained immediately after MRgFUS ablation. The segmentation volume before and after deformation was calculated and compared to determine the final volume change for each subject. A volume change of less than 0.5% was assumed to adequately preserve volume.

V. MULTIPARAMETRIC BIOMARKER CNN

The input data for the MPB-CNN are the pre- and post-MRgFUS ablation MPMR images described in Table I. The label was the follow-up NPV registered with the treatment-day MPMR images according to the AVOCADO algorithm. The objective was to train the MPB-CNN to predict the nonviable tissue using only noncontrast MPMR images acquired pre- and post-MRgFUS ablation. The performance of the MPB-CNN was evaluated by comparing the prediction with the treatment-day NPV, which is a commonly used clinical metric of nonviable tissue. The network was considered successful if its prediction of the nonviable tissue was as accurate or more accurate than the treatment-day NPV as measured by the DICE coefficient [47]. The data set, preprocessing, and neural network architecture for deep learning MR biomarkers are described here.

A. Data Set and Preprocessing

The training data for MPB-CNN was selected from the results of AVOCADO registration between immediate MPMR and follow-up images. Two subjects were excluded from the MPB-CNN set due to small follow-up NPV volumes, leaving $N=6$ animals for MPB-CNN data. In the six subjects used for training and validation, there was no notable growth in the tumor size in the 3-5 day period following treatment. Each acute MR image was resampled with linear interpolation onto a common grid with 0.5 mm isotropic resolution to accommodate the subset of immediate MPMR images acquired at lower resolutions. The target label for each subject was the expert segmentation of the follow-up NPV deformed with the subject-specific diffeomorphism from AVOCADO, which results in a common grid for all the real-time MR images and target images for each subject.

The six MR images input to the network were 2D slices from: (1) pre- and (2) postablation T2w images, (3) pre- and (4) postablation apparent diffusion coefficient (ADC) maps, (5) cumulative thermal dose (CTD) map, and (6) a maximum temperature projection (MTP) map, derived from MR temperature imaging. Although not inclusive of all MPMR contrasts, these inputs were chosen due to the resolution achievable in reasonable time limits (5-10 minutes per contrast) and prior work showing changes in these parameters to be indicative of ablation damage [13]. The ADC maps were calculated from diffusion weighted imaging using the MRI vendor's proprietary image reconstruction pipeline (Siemens, Erlangen, Germany). The CTD maps were calculated from MRTI using the equivalent number of minutes of heating at 43 °C relationship commonly used for thermal therapies [48], [49]. The MTP maps were the highest temperature recorded for each pixel from the MRTI over time (using a rectal probe for starting temperature).

All images were cropped to a $128 \times 128 \times 90$ region centered on the registered follow-up NPV segmentation, and image intensities were normalized using the average maximum from

that image type across all subjects (e.g., the average maximum ADC map value across all subjects is used to normalize all the ADC maps, etc.). The center slice along the last dimension of each $128 \times 128 \times 90$ volume was extracted for evaluation. However, the slices adjacent to the center slice are too similar to the evaluation slice to include in the training data. The four slices on either side of the evaluation slice were omitted from the testing and training data in an attempt to ensure the network is not biased. As a result, we had 486 ($[90 - 9] \times 6$ animals) 128×128 2D samples for training and 6 128×128 2D samples for evaluation. Each input training batch was augmented with: 1) 0-10% random changes in the brightness, contrast, and saturation; 2) random horizontal and vertical flips; 3) random rotations of 0-20 degrees; and 4) zero mean Gaussian noise.

B. Network Architecture

A U-Net segmentation architecture was used for the MPB-CNN with six input channels [50]. In addition to the superior performance of U-Net compared to other CNN architectures, this architecture has demonstrated success with a small number of training samples, making it ideal for the MPB-CNN. The network returned a pixel-wise probability of the tissue viability, and the output of the network was evaluated against the follow-up NPV segmentation using a binary cross entropy loss function. The network was validated with the central slice from each input volume slab (which was excluded from the training data). When evaluating the network, the probability output from the network was thresholded at a value of 0.5 to yield a segmentation of viable versus nonviable tissue. The purpose of the MPB-CNN was to provide a more accurate and immediate prediction of treated tissue than the treatment-day NPV biomarker without using CE imaging. Comparison of the MPB-CNN biomarker with the treatment day NPV biomarker was computed by the DICE coefficient between each MPB-CNN prediction against the follow-up NPV segmentation.

VI. RESULTS

The overall goal of registration was to align the follow-up NPV with the acute MR imaging obtained immediately after MRgFUS ablation while preserving volume. Figure 5 shows a 2D slice of the 3D deformation grid from both DRAMMS and AVOCADO and the corresponding relative volume change (Jacobian determinant) of each field. Both methods were executed on the same noncontrast source and target images. The left column shows the target (top) and source (bottom) noncontrast images, the middle column shows the deformation grid, and the right column shows the Jacobian determinant, which indicates volume change relative to the starting volume. Note that AVOCADO produces a smoother deformation grid and preserves the original volume (Jacobian determinant of 1.0).

A. Registration Accuracy

The final TRE for DRAMMS and AVOCADO is plotted in Figure 6. For the eight rabbits analyzed in this study, the final TRE for AVOCADO ranged from 1.08 mm to 1.60 mm (mean \pm STD = 1.33 ± 0.16 mm). For DRAMMS, the final TRE ranged from 1.07 mm to 2.78 mm (1.69 ± 0.64 mm). An

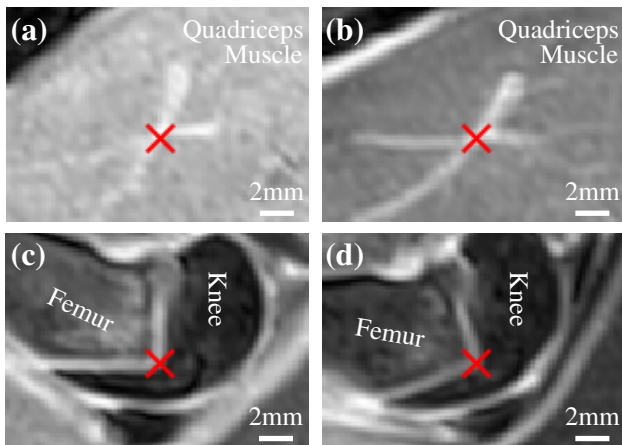


Fig. 4: Example validation landmarks: (a) and (b) show a corresponding blood vessel bifurcation in the treatment and follow-up CE images, respectively, that was not visible during registration; and (c) and (d) show a corresponding bone structure in the treatment and follow-up images, respectively, that was visible during registration.

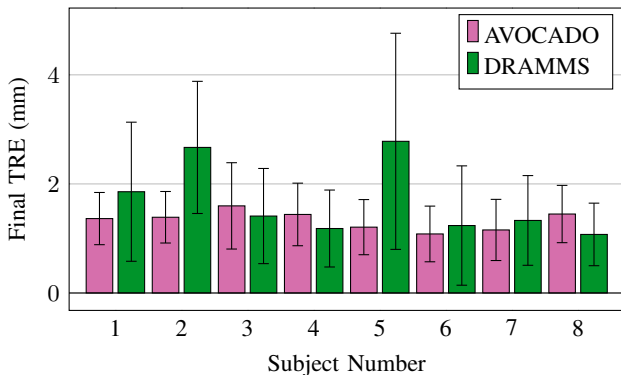


Fig. 6: Plot of the TRE for both non-volume-preserving (DRAMMS) and volume-preserving (AVOCADO) registration methods.

example of the deformations produced from DRAMMS and AVOCADO can be seen in Figure 5. The deformations ϕ^{-1} from AVOCADO are smoother than from DRAMMS, and the Jacobian determinant for AVOCADO is 1.0 over the entire volume. The TRE for AVOCADO was significantly lower than DRAMMS ($p = 0.018$) while preserving the original volume of the anatomies.

The intra-observer variability for the validation landmarks over the eight rabbits ranged from 0.82 mm to 1.22 mm (0.93 ± 0.13 mm). The inter-observer variability ranged from 0.65 mm to 1.26 mm (0.89 ± 0.18 mm). There was no significant difference between the inter-observer and intra-observer errors ($p = 0.95$).

B. User-Dependent Model Inputs

Figure 7 shows the results of perturbing the RBF initialization landmarks. For perturbations under the average user-repeatability (intraobserver) error, the final TRE changed minimally. As expected, if the perturbations became large (> 2 mm), the final TRE also increased.

C. Volume Preservation

The original volumes, deformed volumes, and the percent change for both the non-volume-preserving (DRAMMS) and volume-preserving (AVOCADO) registration methods are reported in Table III. The original volume of the expert NPV biomarker segmented on follow-up CE T1w MR imaging

ranged from 0.02 ml to 3.96 ml (1.34 ± 1.39 ml). The absolute volume change after registration with AVOCADO ranged from 0.07% to 0.39% ($0.28 \pm 0.11\%$). All volume changes for AVOCADO are under our 0.5% threshold for discretization or interpolation error.

In every subject, registration with DRAMMS caused a larger change in the follow-up NPV segmentation volume when compared to the AVOCADO results. The average absolute volume change of the NPV biomarker due to registration with

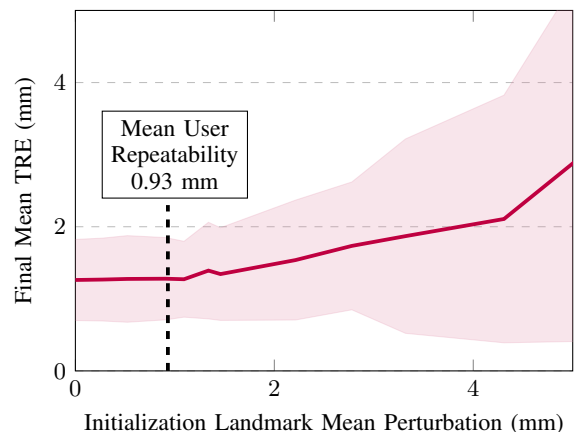


Fig. 7: Mean anatomical perturbation across all subjects plotted versus the final mean TRE of the registration. The mean intraobserver variability for selecting anatomical landmarks is 0.93 mm.

TABLE III: Volumes and changes from non-volume-preserving (DRAMMS) and volume-preserving (AVOCADO) registration. A negative percent means a reduction in the final volume.

Subj.	Original	DRAMMS		AVOCADO	
	Vol mm^3	Vol mm^3	%	Vol mm^3	%
1	1334.75	905.31	-32.17	1339.66	0.37
2	38.00	55.77	46.76	38.13	0.34
3	915.38	903.44	-1.30	911.82	-0.39
4	161.00	145.09	-9.88	161.57	0.36
5	20.38	12.61	-38.11	20.42	0.22
6	1949.15	1614.37	-17.18	1955.99	0.35
7	2628.12	3268.78	24.38	2629.99	0.07
8	3959.38	3878.74	-2.04	3966.28	0.17

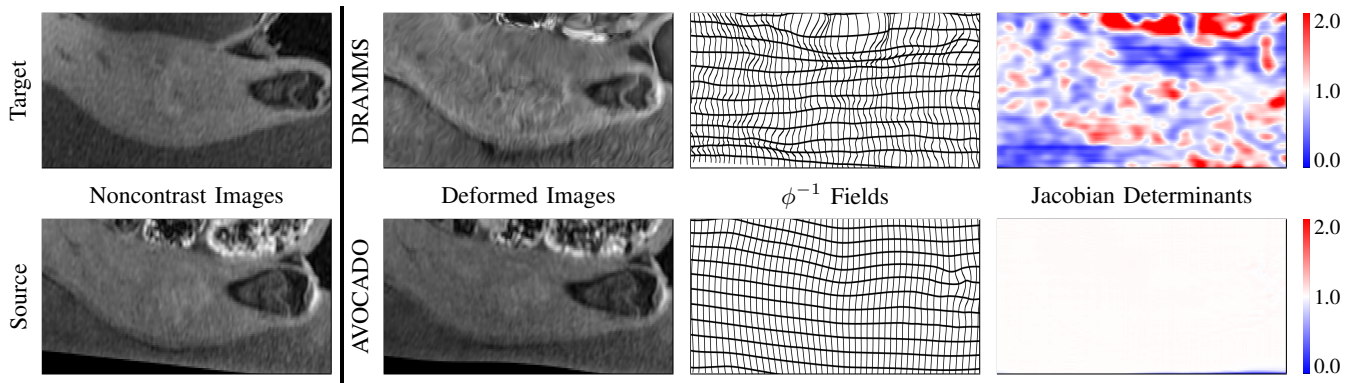


Fig. 5: Subject-specific (subject 7) comparison of DRAMMS and AVOCADO deformation fields. The first column shows the noncontrast source and target images used for registration. The second column shows the deformation field produced by DRAMMS (top) and AVOCADO (bottom) after registering the source and target images. Note the smoothness of the deformation and homogeneity of the Jacobian determinant produced by AVOCADO.

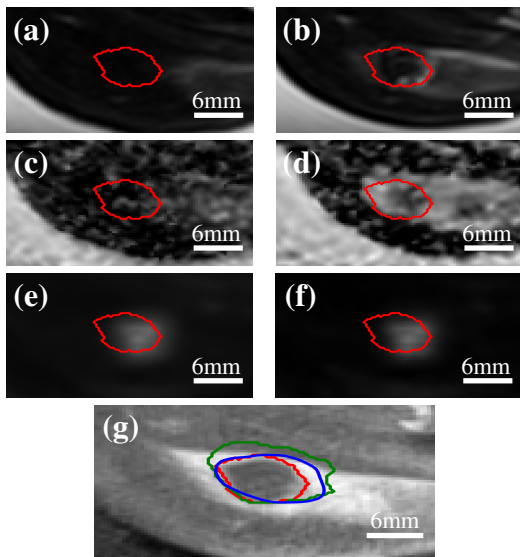


Fig. 8: CNN prediction example for subject 7. Normalized input parameters to the network include: (a) pre-T2w, (b) post-T2w, (c) pre-ADC map, (d) post-ADC map, (e) CTD map, and (f) MTP map. The red line on each input parameter shows the registered follow-up NPV contour. (g) The follow-up NPV contour (red), the acute NPV prediction (green), and the CNN prediction (blue).

TABLE IV: DICE comparison between the MPB-CNN biomarker and the Acute NPV biomarker for each subject (subjects 2 and 5 were excluded). Each biomarker was compared against the Day 3-5 NPV label. The best DICE score for each subject is bold.

Marker	Subject						Mean \pm Std.
	1	3	4	6	7	8	
Acute NPV	0.83	0.71	0.00	0.23	0.70	0.70	0.53 \pm 0.30
MPB-CNN	0.86	0.65	0.30	0.80	0.86	0.77	0.71 \pm 0.21

DRAMMS ranged from 1.30% to 46.76% (21.48 ± 16.80 %). DRAMMS registration resulted in both increased or decreased NPV biomarker volume, with the largest increase of 46.47% and the largest decrease of 38.11%.

D. MPB-CNN

An example of the prediction from the biomarker CNN on one of the validation images is shown in Figure 8. Images (a)-(f) show the six input channels to the network with the registered follow-up NPV contour overlaid in red. The bottom image (g) shows the prediction using acute NPV (green contour) versus using the trained biomarker CNN (blue contour) against the follow-up NPV (red contour). The network yields a more accurate prediction of the final treated tissue than the acute NPV. The DICE coefficient of the acute NPV prediction compared with the follow-up NPV over all validation images ranged from 0.00 to 0.83 (0.53 ± 0.30), whereas the DICE coefficient of the MPB-CNN prediction compared with the follow-up NPV over all validation images ranged from 0.30 to 0.86 (0.71 ± 0.21). The DICE coefficient comparisons on a subject-by-subject basis are shown in Table IV.

VII. DISCUSSION

The results of MPB-CNN show that noncontrast, multiparametric MR biomarkers acquired during the treatment are more reliable for assessing MRgFUS treated tissue than the clinical NPV biomarker. The MPB-CNN was able to better predict the treated tissue seen on follow-up imaging than the clinical treatment-day NPV biomarker for five out of six subjects. The prediction was based on MR images that do not require gadolinium contrast agents. This allows treatment to continue following assessment without the risk of trapping toxic contrast agent in the tissue. Additionally, the total MR acquisition time of the MPMR images was only ~ 5.5 minutes, which is well within expected time limits for an assessment protocol [12].

The MPB-CNN prediction could be improved with additional MR parameters such as quantitative T1 or T2 mapping. The intrinsic T1 and T2 relaxation times are influenced by HIFU-induced changes that could correlate with tissue viability. Several studies have reported significant changes in T1, T2, and ADC values after thermal ablation [12]. These properties are sensitive to post-treatment tissue changes such as hemorrhage, edema, intra- and extra-cellular water content, which may correlate with tissue viability [12]. Although T1- and T2-weighted images are sensitive to these changes in relaxation times, their signal intensities are only relatively quantifiable and dependent on magnet strength, vendor, B0 drift, and scanning parameters. In contrast, quantitative T1 and T2 mapping provide intrinsic tissue properties independent of these factors. Therefore, quantitative inputs to the MPB-CNN may be more easily generalizable across patients or even studies. There is an ongoing, considerable effort in the field of MR to improve standardization and acquisition time of quantitative maps. Improved MR sequences are being developed to simultaneously acquire these MR contrasts to eliminate the least predictive input scans and optimize scan time [51].

General-purpose registration methods, such as DRAMMS, can cause volume change during registration, as shown in Table III. Even though the ablation volume was not visible in the source and target registration volumes, DRAMMS still introduced volume changes to these regions. The average volume change over the 8 subjects using DRAMMS was 21.48%. These volume changes are not plausible and are an artifact of the DRAMMS registration algorithm. If registration introduces a volume artifact, it will directly affect the prediction of the treatment outcome. If the volume of the follow-up NPV is increased or decreased during registration, the MPB-CNN would be trained to similarly over- or underestimate the nonviable tissue. AVOCADO constrains volume change so the original volume of the follow-up NPV did not change after applying the diffeomorphism. This deformation model is more physiologically relevant because tissues do not change volume during deformation. In addition to preserving the volume, our registration method out-performed registration accuracy of state-of-the-art DRAMMS registration method for this task.

Longitudinal registration of MRgFUS images still presents several challenges. The water used for acoustic coupling to

the quadriceps created a large homogeneous intensity on the MR images, which causes automatic affine registration to favor matching the water signal as opposed to the quadriceps. Additionally, due to the rabbit being positioned on its side, the delineation between bladder and the quadriceps was often unclear, which made registration of just the quadriceps difficult. Although we encountered several registration challenges with the chosen model, MRgFUS ablation therapies are being investigated in application to other anatomies, including breast, brain, and prostate. With other anatomies, challenges specific to this study (such as the delineation between bladder and quadriceps) will not affect the registration; however, similar anatomy-specific issues may require individual attention. For example, in abdominal applications, changes in bladder fluid levels and bowel contents may induce volume changes in the images. Using patient-specific segmentations, AVOCADO can be easily extended to have a spatially varying volume preservation using the segmentations to define $\alpha(x)$ in Equation 8 to not constrain regions of the image undergoing known volume change, such as the fluid in the bladder. This would allow volume preserving registration in the ablated tissue regions between images with large volume changes due to contents of the bowel or bladder.

Despite these limitations, AVOCADO demonstrated that registration with volume conservation does not inhibit the accuracy of registration. Conversely, AVOCADO outperformed DRAMMS because it produced deformations that are more indicative of physiological changes in patient position and pose. Whereas this study was implemented on a MRgFUS data set, the registration pipeline is generalizable to other longitudinal imaging studies with both therapeutic and diagnostic implications where volume preservation may be needed.

Although this initial MPB-CNN study presents promising results, it still had limitations. We recognize that the network presented here was trained using limited data. Obtaining data for a single subject to train the network is cumbersome and expensive. With limited retrospective data, the focus was on developing a promising network. However, future studies need to utilize the MPB-CNN to predict tissue viability following an ablation procedure and compare against the NPV biomarker 3-5 days later to fully test the efficacy of the network on subjects independent of training subjects. Additional data would allow for training more accurate and generalizable models. However, this work demonstrates that a CNN approach can provide more accurate measures of the treated tissue compared to traditional methods. Comparing immediate MPMR biomarkers with the follow-up NPV is a necessary intermediate step toward defining new immediate MPMR biomarkers for treatment assessment.

Although the MPB-CNN performed better than the NPV biomarker in predicting tissue necrosis, the performance must still be improved to be an accurate biomarker for malignant tumors. Future work will include adding additional input features to improve the prediction accuracy and subsequently analyzing the MPB-CNN to determine the inputs that provide the most predictive power for the network. With a better understanding of the optimal input features, the network could be retrained to provide a more accurate prediction of the

treated tissue. By understanding the network weights, the underlying intrinsic tissue property that is the best indicator of tissue viability could be determined. Gaining this insight will allow the design of a more targeted MR protocol and modify the network inputs to maximize the predictive power of the MPB-CNN. Although the presented registration has been applied to a specific animal model and data, the methods can be expanded to investigate and improve other minimally and noninvasive MR guided treatments.

ACKNOWLEDGEMENTS

We would like to acknowledge Robb Merrill, Hailey McLean, and Elaine Hillas for their contributions.

REFERENCES

- [1] M. A. Haider *et al.*, "Dynamic contrast-enhanced magnetic resonance imaging for localization of recurrent prostate cancer after external beam radiotherapy," *International Journal of Radiation Oncology* Biology* Physics*, vol. 70, no. 2, pp. 425–430, 2008.
- [2] O. Rouvière, A. Gelet, S. Crouzet, and J.-Y. Chapelon, "Prostate focused ultrasound focal therapy—imaging for the future," *Nature Reviews Clinical Oncology*, vol. 9, no. 12, p. 721, 2012.
- [3] A. P. Kirkham, M. Emberton, I. M. Hoh, R. O. Illing, A. A. Freeman, and C. Allen, "Mr imaging of prostate after treatment with high-intensity focused ultrasound," *Radiology*, vol. 246, no. 3, pp. 833–844, 2008.
- [4] E. A. Stewart *et al.*, "Focused ultrasound treatment of uterine fibroid tumors: safety and feasibility of a noninvasive thermoablative technique," *American journal of obstetrics and gynecology*, vol. 189, no. 1, pp. 48–54, 2003.
- [5] C. M. Tempany, E. A. Stewart, N. McDannold, B. J. Quade, F. A. Jolesz, and K. Hynynen, "Mr imaging-guided focused ultrasound surgery of uterine leiomyomas: a feasibility study," *Radiology*, vol. 226, no. 3, pp. 897–905, 2003.
- [6] G. K. Hesley, K. R. Gorny, and D. A. Woodrum, "Mr-guided focused ultrasound for the treatment of uterine fibroids," *Cardiovascular and interventional radiology*, vol. 36, no. 1, pp. 5–13, 2013.
- [7] D. Gianfelice, C. Gupta, W. Kucharczyk, P. Bret, D. Havill, and M. Clemons, "Palliative treatment of painful bone metastases with mr imaging-guided focused ultrasound," *Radiology*, vol. 249, no. 1, pp. 355–363, 2008.
- [8] F. Zaccagna *et al.*, "Palliative treatment of painful bone metastases with mr imaging-guided focused ultrasound surgery: a two-centre study," *Journal of therapeutic ultrasound*, vol. 3, no. 1, p. O51, 2015.
- [9] T. Leslie *et al.*, "High-intensity focused ultrasound ablation of liver tumours: can radiological assessment predict the histological response?" *The British journal of radiology*, vol. 81, no. 967, pp. 564–571, 2008.
- [10] J. Wijlemans *et al.*, "Magnetic resonance-guided high-intensity focused ultrasound (mr-hifu) ablation of liver tumours," *Cancer Imaging*, vol. 12, no. 2, p. 387, 2012.
- [11] M. S. Sabel *et al.*, "Cryoablation of early-stage breast cancer: work-in-progress report of a multi-institutional trial," *Annals of surgical oncology*, vol. 11, no. 5, pp. 542–549, 2004.
- [12] S. J. Hectors, I. Jacobs, C. T. Moonen, G. J. Strijkers, and K. Nicolay, "Mri methods for the evaluation of high intensity focused ultrasound tumor treatment: Current status and future needs," *Magnetic resonance in medicine*, vol. 75, no. 1, pp. 302–317, 2016.
- [13] S. J. Hectors, I. Jacobs, G. J. Strijkers, and K. Nicolay, "Multiparametric mri analysis for the identification of high intensity focused ultrasound-treated tumor tissue," *PloS one*, vol. 9, no. 6, p. e99936, 2014.
- [14] A. Payne *et al.*, "In vivo evaluation of a breast-specific magnetic resonance guided focused ultrasound system in a goat udder model," *Medical physics*, vol. 40, no. 7, 2013.
- [15] J. W. Wijlemans *et al.*, "Evolution of the ablation region after magnetic resonance-guided high-intensity focused ultrasound ablation in a vx2 tumor model," *Investigative radiology*, vol. 48, no. 6, pp. 381–386, 2013.
- [16] N. McDannold *et al.*, "Uterine leiomyomas: Mr imaging-based thermometry and thermal dosimetry during focused ultrasound thermal ablation," *Radiology*, vol. 240, no. 1, pp. 263–272, 2006.
- [17] N. M. Hijnen, A. Elevelt, and H. Grull, "Stability and trapping of magnetic resonance imaging contrast agents during high-intensity focused ultrasound ablation therapy," *Investigative radiology*, vol. 48, no. 7, pp. 517–524, 2013.

- [18] N. M. Hijnen, A. Elevelt, J. Pikkemaat, C. Bos, L. W. Bartels, and H. Gröll, "The magnetic susceptibility effect of gadolinium-based contrast agents on prfs-based mr thermometry during thermal interventions," *Journal of therapeutic ultrasound*, vol. 1, no. 1, p. 8, 2013.
- [19] J. C. Plata *et al.*, "A feasibility study on monitoring the evolution of apparent diffusion coefficient decrease during thermal ablation," *Medical physics*, vol. 42, no. 9, pp. 5130–5137, 2015.
- [20] L. Mannelli, S. Kim, C. H. Hajdu, J. S. Babb, T. W. Clark, and B. Taouli, "Assessment of tumor necrosis of hepatocellular carcinoma after chemoembolization: diffusion-weighted and contrast-enhanced mri with histopathologic correlation of the explanted liver," *American Journal of Roentgenology*, vol. 193, no. 4, pp. 1044–1052, 2009.
- [21] Q. Wu, G. J. Whitman, D. S. Fussell, and M. K. Markey, "Registration of dce mr images for computer-aided diagnosis of breast cancer," in *2006 Fortieth Asilomar Conference on Signals, Systems and Computers*. IEEE, 2006, pp. 826–830.
- [22] Y. Ou, A. Sotiras, N. Paragios, and C. Davatzikos, "Dramms: Deformable registration via attribute matching and mutual-saliency weighting," *Medical image analysis*, vol. 15, no. 4, pp. 622–639, 2011.
- [23] X. Li *et al.*, "A nonrigid registration algorithm for longitudinal breast mr images and the analysis of breast tumor response," *Magnetic resonance imaging*, vol. 27, no. 9, pp. 1258–1270, 2009.
- [24] K. K. Brock, L. A. Dawson, M. B. Sharpe, D. J. Moseley, and D. A. Jaffray, "Feasibility of a novel deformable image registration technique to facilitate classification, targeting, and monitoring of tumor and normal tissue," *International Journal of Radiation Oncology* Biology* Physics*, vol. 64, no. 4, pp. 1245–1254, 2006.
- [25] Y. Ou *et al.*, "Deformable registration for quantifying longitudinal tumor changes during neoadjuvant chemotherapy," *Magnetic resonance in medicine*, vol. 73, no. 6, pp. 2343–2356, 2015.
- [26] N. Jahani *et al.*, "Deformable image registration as a tool to improve survival prediction after neoadjuvant chemotherapy for breast cancer: results from the acrin 6657/i-spy-1 trial," in *Medical Imaging 2018: Computer-Aided Diagnosis*, vol. 10575. International Society for Optics and Photonics, 2018, p. 105752S.
- [27] J. D. Humphrey, "Continuum biomechanics of soft biological tissues," *Proceedings of the Royal Society of London. Series A: Mathematical, Physical and Engineering Sciences*, vol. 459, no. 2029, pp. 3–46, 2003.
- [28] B. L. Godwin and J. E. Coad, "Healing responses following cryothermic and hyperthermic tissue ablation," in *Energy-based Treatment of Tissue and Assessment V*, vol. 7181. International Society for Optics and Photonics, 2009, p. 718103.
- [29] T. Rohlfing, C. R. Maurer, D. A. Bluemke, and M. A. Jacobs, "Volume-preserving nonrigid registration of mr breast images using free-form deformation with an incompressibility constraint," *IEEE transactions on medical imaging*, vol. 22, no. 6, pp. 730–741, 2003.
- [30] J. Palussiere *et al.*, "Feasibility of mr-guided focused ultrasound with real-time temperature mapping and continuous sonication for ablation of vx2 carcinoma in rabbit thigh," *Magnetic Resonance in Medicine: An Official Journal of the International Society for Magnetic Resonance in Medicine*, vol. 49, no. 1, pp. 89–98, 2003.
- [31] G. E. Christensen, R. D. Rabbitt, and M. I. Miller, "Deformable templates using large deformation kinematics," *IEEE transactions on image processing*, vol. 5, no. 10, pp. 1435–1447, 1996.
- [32] S. C. Joshi and M. I. Miller, "Landmark matching via large deformation diffeomorphisms," *IEEE transactions on image processing*, vol. 9, no. 8, pp. 1357–1370, 2000.
- [33] Y. Guo and C.-C. Lu, "Multi-modality image registration using mutual information based on gradient vector flow," in *18th International Conference on Pattern Recognition (ICPR'06)*, vol. 3. IEEE, 2006, pp. 697–700.
- [34] S. Haker, L. Zhu, A. Tannenbaum, and S. Angenent, "Optimal mass transport for registration and warping," *International Journal of computer vision*, vol. 60, no. 3, pp. 225–240, 2004.
- [35] M. Bauer, M. Bruveris, and P. W. Michor, "Overview of the geometries of shape spaces and diffeomorphism groups," *Journal of Mathematical Imaging and Vision*, vol. 50, no. 1-2, pp. 60–97, 2014.
- [36] L. Younes, *Shapes and diffeomorphisms*. Springer, 2010, vol. 171.
- [37] G. Misiolek, "Stability of flows of ideal fluids and the geometry of the group of diffeomorphisms," *Indiana University mathematics journal*, pp. 215–235, 1993.
- [38] J. Hinkle, M. Szegedi, B. Wang, B. Salter, and S. Joshi, "4d ct image reconstruction with diffeomorphic motion model," *Medical image analysis*, vol. 16, no. 6, pp. 1307–1316, 2012.
- [39] H. Bhatia, G. Norgard, V. Pascucci, and P.-T. Bremer, "The helmholtz-hodge decomposition—a survey," *IEEE Transactions on visualization and computer graphics*, vol. 19, no. 8, pp. 1386–1404, 2012.
- [40] J. Cantarella, D. DeTurck, and H. Gluck, "Vector calculus and the topology of domains in 3-space," *The American mathematical monthly*, vol. 109, no. 5, pp. 409–442, 2002.
- [41] C. F. Van Loan and G. H. Golub, *Matrix computations*. Johns Hopkins University Press, 1983.
- [42] M. D. Buhmann, *Radial basis functions: theory and implementations*. Cambridge university press, 2003, vol. 12.
- [43] M. F. Beg, M. I. Miller, A. Trounev, and L. Younes, "Computing large deformation metric mappings via geodesic flows of diffeomorphisms," *International journal of computer vision*, vol. 61, no. 2, pp. 139–157, 2005.
- [44] A. Fedorov *et al.*, "3d slicer as an image computing platform for the quantitative imaging network," *Magnetic resonance imaging*, vol. 30, no. 9, pp. 1323–1341, 2012.
- [45] Y. Ou, H. Akbari, M. Bilello, X. Da, and C. Davatzikos, "Comparative evaluation of registration algorithms in different brain databases with varying difficulty: results and insights," *IEEE transactions on medical imaging*, vol. 33, no. 10, pp. 2039–2065, 2014.
- [46] Y. Ou, D. H. Ye, K. M. Pohl, and C. Davatzikos, "Validation of dramms among 12 popular methods in cross-subject cardiac mri registration," in *International Workshop on Biomedical Image Registration*. Springer, 2012, pp. 209–219.
- [47] L. R. Dice, "Measures of the amount of ecologic association between species," *Ecology*, vol. 26, no. 3, pp. 297–302, 1945.
- [48] G. C. Van Rhoon, T. Samaras, P. S. Yarmolenko, M. W. Dewhirst, E. Neufeld, and N. Kuster, "Cem43° c thermal dose thresholds: a potential guide for magnetic resonance radiofrequency exposure levels?" *European radiology*, vol. 23, no. 8, pp. 2215–2227, 2013.
- [49] M. W. Dewhirst, B. Viglianti, M. Lora-Michiels, M. Hanson, and P. Hoopes, "Basic principles of thermal dosimetry and thermal thresholds for tissue damage from hyperthermia," *International journal of hyperthermia*, vol. 19, no. 3, pp. 267–294, 2003.
- [50] O. Ronneberger, P. Fischer, and T. Brox, "U-net: Convolutional networks for biomedical image segmentation," in *International Conference on Medical image computing and computer-assisted intervention*. Springer, 2015, pp. 234–241.
- [51] C.-C. Cheng *et al.*, "Dual-pathway multi-echo sequence for simultaneous frequency and t2 mapping," *Journal of Magnetic Resonance*, vol. 265, pp. 177–187, 2016.